Check for updates

MATERIALS SCIENCE

P- and *N*-type InAs nanocrystals with innately controlled semiconductor polarity

Jong Il Yoon[1]†, Hyoin Kim[2]†, Meeree Kim[2], Hwichan Cho[1], Yonghyun Albert Kwon[3], Mahnmin Choi[2], Seongmin Park[2], Taewan Kim[2], Seunghan Lee[1], Hyunwoo Jo[1], BongSoo Kim[4], Jeong Ho Cho[3], Ji-Sang Park[5]*, Sohee Jeong[2,6]*, Moon Sung Kang[1,7]*

Copyright © 2023 The Authors, some rights reserved; exclusive licensee American Association for the Advancement of Science. No claim to original U.S. Government Works. Distributed under a Creative Commons Attribution NonCommercial License 4.0 (CC BY-NC).

InAs semiconductor nanocrystals (NCs) exhibit intriguing electrical/optoelectronic properties suitable for next-generation electronic devices. Although there is a need for both *n*- and *p*-type semiconductors in such devices, InAs NCs typically exhibit only *n*-type characteristics. Here, we report InAs NCs with controlled semiconductor polarity. Both *p*- and *n*-type InAs NCs can be achieved from the same indium chloride and aminoarsine precursors but by using two different reducing agents, diethylzinc for *p*-type and diisobutylaluminum hydride for *n*-type NCs, respectively. This is the first instance of semiconductor polarity control achieved at the synthesis level for InAs NCs and the entire semiconductor nanocrystal systems. Comparable field-effective mobilities for holes (3.3×10^{-3} cm^2/V·s) and electrons (3.9×10^{-3} cm^2/V·s) are achieved from the respective NC films. The mobility values allow the successful fabrication of complementary logic circuits, including NOT, NOR, and NAND comprising photopatterned *p*- and *n*-channels based on InAs NCs.

Downloaded from https://www.science.org on December 15, 2023

INTRODUCTION

Semiconductor nanocrystals (NCs) with size-dependent tunable electronic properties are attractive building blocks for future electronic devices (*1*). Despite the great opportunities, the benchmark NC systems developed so far typically include hazardous Cd, Pb, or Hg that violate the rigorous RoHS requirement (*2*). In-based NCs are attractive alternatives to these NC systems, not only because they avoid hazardous elements but also because they exhibit more stable physical characteristics due to the stronger covalent nature of III-V bonding (*3*, *4*). For example, InP-based NCs are already the core materials of commercial quantum dot displays (*5*, *6*). More recently, InAs NCs have drawn substantial research interest based on intriguing materials properties, including large optical extinction in the near-infrared to the short-wavelength infrared regime and high charge carrier mobility for advanced electronics applications (*7*–*11*). However, the polarity control of the semiconductor characteristics for these materials has hardly been performed. The as-synthesized InAs NCs (as well as InP NCs) reported so far are limited to exhibiting *n*-type semiconductor characteristics and attaining *p*-type characteristics remains a challenge (*7*–*9*, *12*–*15*). The dominant *n*-type semiconductor characteristics from InAs NCs are attributed to the inherent donor-like defects formed on the InAs surface that pin the Fermi level close to the conduction band minimum (CBM) (*16*, *17*); this impact would be amplified for NCs with large surface areas.

The challenge of attaining RoHS compliant *p*-type InAs NCs prevents their practical application of these NC systems in various optoelectronic devices. It is well agreed that complementary circuits based on *p*- and *n*-type channels permit the design of simpler and efficient logic gates (*18*–*20*) and that *p*-*n*-junction serves as the basic building blocks for efficient optoelectronic devices such as photodiodes or photovoltaics (*21*–*23*). Even the InAs NC photovoltaics in the literature only use the materials as the *n*-type layer while still employing lead chalcogenides as the *p*-type counterpart (*9*). Very recently, attempts have been made to dope InAs NCs into *p*-type by introducing heterovalent atoms within the lattice. However, the reported studies either used toxic Cd as the dopant or used complicated postsynthetic doping steps, which only resulted in moderate hole mobilities (*24*–*26*). *P*-type InAs NCs with hole mobility comparable to their *n*-type counterpart have been hardly achieved. Overall, a strategy to innately control the semiconductor polarity type of InAs NCs from the synthesis level is highly sought for practical usage of these RoHS-compliant nanomaterials.

Here, we report InAs NCs exhibiting either *p*-type or *n*-type characteristics, of which the semiconductor polarity is innately determined by the synthetic step. Both *p*- and *n*-type InAs NCs yielding comparable hole and electron mobilities in assemblies could be synthesized using the same indium chloride and aminoarsine precursors but by exploiting the two different reducing agents needed to release As from the precursor during the nucleation and growth of the crystal. We discovered that diethylzinc (Et_2Zn) as the reducing agent yields *p*-type InAs NCs as Zn serves as a substitutional *p*-type acceptor within the InAs lattice. Meanwhile, a typical reducing agent like diisobutylaluminum hydride (DIBAL-H) resulted in *n*-type InAs NCs, which is consistent with the bulk semiconductor characteristics of InAs. We emphasize that the result is the first polarity control of semiconductor characteristics exploiting heteroatoms from a synthetic approach not only for InAs NCs but also for all

[1]Department of Chemical and Biomolecular Engineering, Sogang University, Seoul 04107, Republic of Korea. [2]Department of Energy Science (DOES), Center for Artificial Atoms, and Sungkyunkwan Institute of Energy Science and Technology (SIEST), Sungkyunkwan University, Suwon 16419, Republic of Korea. [3]Department of Chemical and Biomolecular Engineering, Yonsei University, Seoul 03722, Republic of Korea. [4]Department of Chemistry, Graduate School of Semiconductor Materials and Device Engineering, and Graduate School of Cabon Neutrality, Ulsan National Institute of Science and Technology (UNIST), Ulsan 44919, Republic of Korea. [5]SKKU Advanced Institute of Nanotechnology (SAINT) and Department of Nano Engineering, Sungkyunkwan University, Suwon 16419, Republic of Korea. [6]Department of Future Energy Engineering (DFEE), Sungkyunkwan University, Suwon 16419, Republic of Korea. [7]Institute of Emergent Materials, Ricci Institute of Basic Science, Sogang University, Seoul 04107, Republic of Korea.
*Corresponding author. Email: kangms@sogang.ac.kr (M.S.K), s.jeong@skku.edu (S. J.), jisangpark@skku.edu (J.-S.P.)
†These authors contributed equally to this work.

semiconductor NC systems reported so far. Notably, the opposite semiconductor polarity of these NCs is retained by using various short ligands in their thin film assemblies. Comparable hole and electron mobility values as high as of 3.3×10^{-3} $cm^2/V\cdot s$ and 3.9×10^{-3} $cm^2/V\cdot s$ could be obtained. The hole mobility is by far the highest value attained for InAs NCs. With *p*-type and *n*-type channels available, we demonstrate the fabrication of complementary logic gates (NOT, NOR, and NAND) based on RoHS-compliant, polarity-controlled NC systems without the aid of postsynthetic doping steps.

RESULTS

Two different InAs NCs were synthesized using the same combination of indium chloride ($InCl_3$) and tris(dimethylamino)arsine (DMA-As) precursors in oleylamine (OLA). DMA-As precursors have received recent attention in the synthesis of InAs NCs because of their relatively high stability and ease of handling (*27*–*29*), compared to previous arsenic precursors such as arsine (AsH_3) (*30*, *31*) or tris(trimethylsilyl)arsine (TMS-As) (*32*–*35*). Moreover, DMA-As precursors are known to be less toxic compared to other As precursors (*29*, *36*). The use of DMA-As requires As in the +3 oxidation state to be reduced to the −3 state during the synthesis, and this is done with the aid of a reducing agent. Et_2Zn or DIBAL-H was used to activate the As precursors (Fig. 1A). The alkyl carbanion in Et_2Zn or hydride in DIBAL-H enabled the reduction of As in DMA-As, which triggered the nucleation and growth kinetics of InAs NCs synthesis (*36*). Accordingly, InAs NCs were prepared by injecting the DMA-As precursor solution with either one of the reducing agents into the $InCl_3$ precursor solution at the desired temperature under an inert atmosphere. Scanning transmission electron microscopy images of the resulting NCs and their size histograms are shown in fig. S1. The average sizes of InAs NCs synthesized using Et_2Zn or DIBAL-H were 3.5 ± 0.5 nm and 4.6 ± 0.6 nm, respectively. Materials and Methods contains details on the synthesis and purification steps. Figure 1B shows diffractograms of the two resulting InAs NCs obtained from x-ray diffraction (XRD) measurement. Both diffractograms show that the two InAs NCs have a zinc-blende structure. We also confirm that despite the inclusion of Zn or Al elements from the reducing agents for the synthesis, no separate sets of peaks attributed to the related components were observable. Figure 1C shows the ultraviolet–visible–near infrared (UV-Vis-NIR) absorbance spectrum of these NCs, exhibiting an optical bandgap in the NIR regime. Figure 1 (D and E) shows the transfer characteristics, that is, the drain current (I_D) versus gate voltage (V_G) relation collected at a fixed drain voltage (V_D), of field-effect transistors (FETs) based on thin films of InAs NCs synthesized using Et_2Zn and DIBAL-H as the reducing agent, respectively. For the FETs, Cr/Au contacts were used as the source and drain electrodes. Heavily *n*-doped Si wafer and the thermally grown SiO_2 layer on top served as the gate electrode and dielectric layer of the device, respectively. The NC films were treated with 1,2-ethanedithiol (EDT) to replace the long-insulating OLA ligands (fig. S2), which was required to enhance the electronic coupling between neighboring NCs. A *p*-type modulation of the channel (increased current level at a more negative V_G) is shown in Fig. 1D, whereas an *n*-type modulation of the channel (increased current level at a more positive V_G) is shown in Fig. 1E. The output characteristics of these devices, that is, I_D versus V_D relations collected at different gate voltages, also follow the typical shape of *p*- and *n*-channel characteristics (Fig. 1, F and G, respectively). This drastic difference directly demonstrates that

Downloaded from https://www.science.org on December 15, 2023

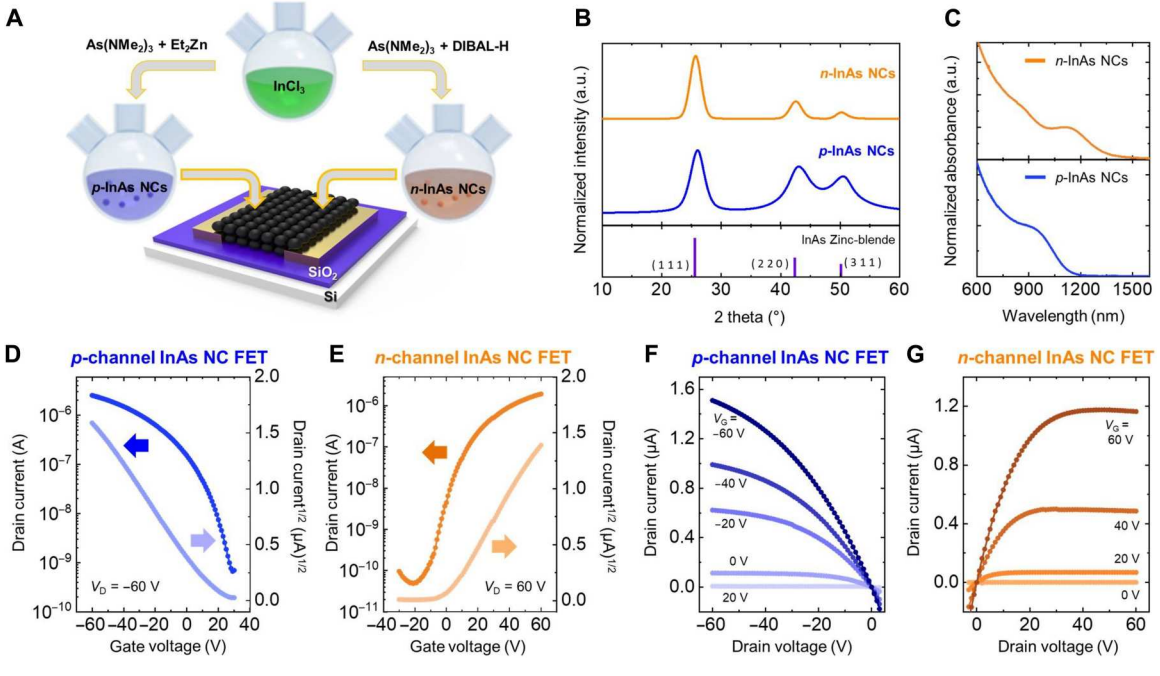

Fig. 1. Synthesis and electrical properties of *p*- and *n*- InAs NCs. (**A**) Schematic of synthetic process for *p*- and *n*-InAs NCs. (**B**) XRD plots for *p*- and *n*-InAs NCs. (**C**) UV-Vis-NIR spectra of the *p*- and *n*-InAs NCs. (**D** and **E**) Transfer characteristics of FETs based on *p*- and *n*-InAs NCs in the saturation region, respectively. (**F** and **G**) Output characteristics of FETs based on *p*- and *n*-InAs NCs. a.u., arbitrary units.

the semiconductor polarity of the InAs NC channels is opposite, such that the InAs NCs synthesized using Et_2Zn are *p*-type. In contrast, those using DIBAL-H are *n*-type. Hereafter, we refer to the NCs synthesized using Et_2Zn and DIBAL-H as *p*- and *n*-InAs NCs, respectively. Comparable (saturation) hole and electron mobility values as high as of 3.3×10^{-3} $cm^2/V\cdot s$ and 3.9×10^{-3} $cm^2/V\cdot s$ could be obtained. The hole mobility is by far the highest value attained for *p*-InAs NCs, respectively. The hole and electron mobility values, along with the threshold voltage of the devices based on the *p*- and *n*-channels, are summarized in Table 1. Note that all the measurements were taken under vacuum conditions. A brief exposure to ambient conditions resulted in a reduction (enhancement) in the current level for *p*-InAs NCs (*n*-InAs NCs), which could be subsequently restored to the original current levels obtained before exposure to ambient through vacuum treatment (fig. S3).

The *n*-type characteristics of the InAs NCs synthesized using DIBAL-H match those typically observed for bulk InAs. For bulk InAs, the surface defects on InAs having formation energy lower than that of bulk defects are known to serve as *n*-type dopants (*16*, *17*). For InAs NCs with a much larger surface area, this inherent *n*-type doping effect was apparent for different ligands introduced at the NC surface (fig. S4). Note that InAs NCs synthesized using TMS-As also show *n*-type characteristics when treated with EDT in the same manner (fig. S5). This is consistent with previous results observed for various InAs NCs prepared using different synthetic protocols (*13*, *24*, *26*). Such a robust *n*-type characteristic for InAs NCs is different from that observed for other NC systems with narrow bandgaps in the NIR, such as PbS or PbSe NCs (the semiconductor polarity for PbS or PbSe NCs is strongly affected by the ligands and surface characteristics) (*37*–*39*). These results indicate that a strong *p*-type dopant is needed to compensate for the inherent *n*-doping effect of InAs NCs and completely convert their semiconductor polarity to *p*-type.

We attribute the drastic contrast in the electrical properties of these InAs NCs to the critical role of Zn provided by Et_2Zn. Specifically, we consider that Zn atoms from Et_2Zn can be incorporated into the InAs lattice during NC growth. Therefore, Et_2Zn in our process acts not only as the reducing agent but also the source of Zn dopant. The presence of Zn in the *p*-InAs NC film was confirmed from x-ray photoelectron spectroscopy (XPS), which was not the case for the *n*-InAs NC film (Fig. 2A). Consistent results were confirmed by energy-dispersive x-ray spectroscopy (fig. S6). This is different from previous reports that used other Zn-containing chemicals during synthesis. For example, when $ZnCl_2$ is included in the synthesis (even in excess amounts), $ZnCl_2$ remains in its salt form. It only functions to passivate the surface dangling bonds of InAs NCs via *Z*-type interaction but does not act as the source of Zn dopant (*36*). In contrast, owing to the strong nucleophilicity of the carbanion, Et_2Zn serves as an effective reducing agent and can be readily decomposed in the synthetic batch to release Zn^{2+}, which would be involved in forming Zn-As bonds during the nucleation and growth of crystals.

We conjecture that the as-incorporated Zn acted as an effective *p*-type dopant for the InAs host. Here, Zn in InAs can either substitute the In site in the lattice or incorporate into the interstitial position of the lattice (Fig. 2B). These two possibilities could be compared based on the formation energy calculations on Zn defects (substitutional defects and interstitial defects) in the InAs lattice through density functional theory (DFT) analysis (*40*). Details of the calculations are described in the Supporting Materials. Figure 2C shows the resulting formation energy for Zn defects with different charge states (z from −1 to +2) in InAs NCs with different Fermi energy (E_F) levels [the position of the E_F for the InAs NCs is depicted relative to the valence band maximum (VBM) position]. For intrinsic InAs NCs (with their E_F near the center of the bandgap), the formation energy for substitutional Zn defects replacing In (red line) was lower than that for interstitial Zn defects (blue line). In particular, substitutional Zn defects with $z = -1$ (indicating that they accept electrons from the lattice or donate holes to the lattice) can be formed at the lowest energy cost. This observation is consistent with a simple valence electron model, suggesting that Zn, with one less valence electron than In, can serve as an electron acceptor for InAs by substitution. Accordingly, the E_F position of the InAs NC will be lowered with the addition of Zn until E_F reaches the condition where the substitutional defects with $z = 0$ yield the lowest energy cost for formation. The condition $z = 0$ indicates that Zn does not accept electrons, and therefore, once $z = 0$ is reached, the addition of Zn does not affect the position of E_F. Accordingly, we can assign this position to the acceptor level of the InAs NCs with Zn substitution. The resulting *p*-type characteristics of the Zn-doped InAs NCs are consistent with our experimental findings shown in Fig. 1 (D and F). The *p*-type electrical characteristics were consistently observed for a series of *p*-InAs NC channels

Table 1. FET characteristics based on *n*- and *p*-InAs NCs (linear and saturation mobility, threshold voltage, subthreshold swing, and on/off ratio). The mobility values were calculated using the typical transistor equations. The specific capacitance of SiO_2 and Al_2O_3 dielectric layer was 11.5 and 100 nF/cm^2, respectively. Data were averaged from more than five devices, and the error bar represents the SD of the data.

Channel	Gate dielectric	Linear mobility ($cm^2/V\cdot s$)	Saturation mobility ($cm^2/V\cdot s$)	Threshold voltage (V)	Subthreshold swing (V/dec)	On/off ratio
p-InAs NCs	SiO_2	$(2.3 \pm 0.2) \times 10^{-3}$	$(3.3 \pm 0.3) \times 10^{-3}$	18.8 ± 0.9	8.1 ± 0.1	$(4.3 \pm 0.5) \times 10^3$
n-InAs NCs	SiO_2	$(3.9 \pm 0.8) \times 10^{-3}$	$(3.9 \pm 0.8) \times 10^{-3}$	2.0 ± 0.8	9.8 ± 1.9	$(1.6 \pm 1.2) \times 10^4$
p-InAs NCs	Al_2O_3	$(4.1 \pm 0.4) \times 10^{-3}$	$(4.4 \pm 0.3) \times 10^{-3}$	0.4 ± 0.1	1.2 ± 0.1	$(1.6 \pm 0.8) \times 10^4$
n-InAs NCs	Al_2O_3	$(2.2 \pm 0.1) \times 10^{-3}$	$(2.6 \pm 0.1) \times 10^{-3}$	1.2 ± 0.1	0.8 ± 0.4	$(7.5 \pm 4.7) \times 10^2$

Downloaded from https://www.science.org on December 15, 2023

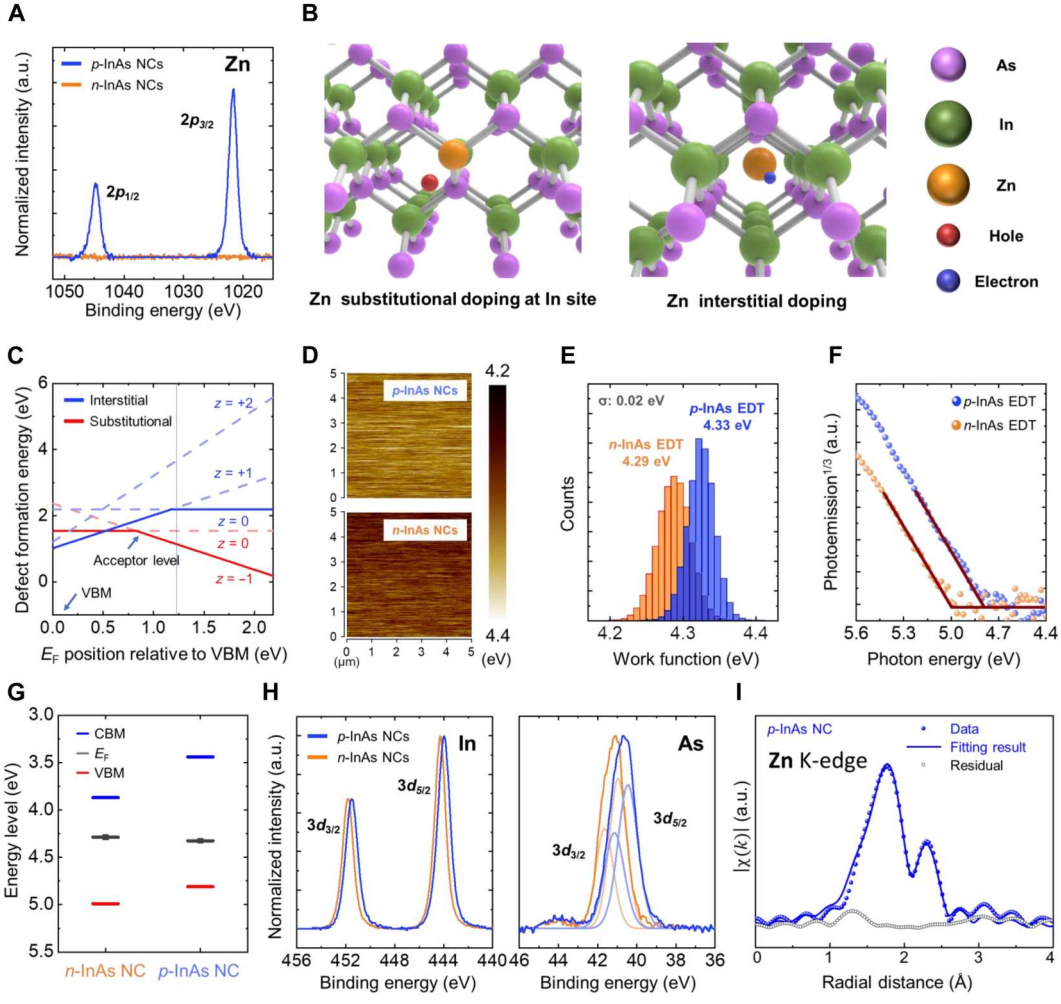

Fig. 2. Structural and electronic characteristics of *p*- and *n*- InAs NCs. (**A**) High-resolution Zn XPS spectrum for *p*- and *n*-InAs NCs. (**B**) Substitutional and interstitial doping model for InAs NCs with Zn. (**C**) Formation energy for Zn defects with different values of *z* in InAs NCs having different E_Fs (the E_F position for the InAs NCs is depicted relative to the VBM position). The calculation was done for the InAs lattice with 79 In and 80 As atoms. The blue and red lines represent the formation energy of interstitial Zn defects within the lattice and substitutional Zn defects replacing In, respectively. (**D**) Maps of surface potential obtained using Kelvin probe force microscopy for EDT-treated films of *p*- and *n*-InAs NCs. (**E**) Histogram of the surface potential values in (D). (**F**) Ambient pressure photoelectron yield spectroscopy spectra of *p*- and *n*-InAs NC films. Linear extrapolation provides the position of the VBM for the given NC films. (**G**) Energy diagram of *p*- and *n*-InAs NC films. (**H**) High-resolution In (left) and As (right) XPS spectra for *p*- and *n*-InAs NCs. (**I**) Zn K-edge EXAFS spectra for p-InAs NCs.

treated with different chemicals to replace/remove ligands, leading to different surface properties (fig. S7). Note that substitutional doping of Zn onto InAs nanowires was reported by Ford *et al.* (*41*), who demonstrated a transition in the electrical characteristics from originally *n*-type to *p*-type upon exposure of the nanowire to Zn vapor.

The presence of Zn resulted in a drastic contrast in the energy levels. The position of E_F was determined using Kelvin probe force microscopy. For ideal semiconductors heavily doped with acceptors and donors, the offset between their E_F can be as large as the bandgap. However, this was not the case for *p*- and *n*-InAs NCs. Figure 2D shows the 5 μm by 5 μm surface potential maps of *n*- and *p*-InAs NC films. Figure 2E shows a histogram of the surface potential values shown in Fig. 2D for these films. E_F of the *p*-InAs NC film was estimated to be 4.33 eV and that of the *n*-InAs NC film was 4.29 eV (SDs were 0.02 eV for both *p*- and *n*-InAs NCs). Despite the drastic contrast in the electrical transport characteristics shown in Fig. 1, their E_F resides at a similar position, which deviates from the ideal behavior explained above. This can be explained by analyzing the Fermi level pinning effect widely observed for semiconductors with numerous defect states (*42*); an offset in the E_F as small as 0.07 eV was observed experimentally even for a set of *n*- and *p*-type doped silicon that have donor and acceptor density of 4×10^{15} cm^{-3} and 1×10^{16} cm^{-3}, respectively, when pinning effect plays a critical role (*42*).

In such cases, the type of semiconductor polarity can be determined based on the relative position of E_F from the VBM or CBM (*42*). The VBM of our NCs was obtained using ambient-pressure photoelectron yield spectroscopy (PYS) (*43*, *44*). Figure 2F plots the counts of photoelectrons protruding from the *p*- and *n*-InAs NCs films under UV irradiation as a function of the respective photon energy. The position of the VBM was determined from

Downloaded from https://www.science.org on December 15, 2023

the energy threshold at which the photon counts increased drastically. The position of CBM was determined simply by using the optical bandgap of the material as an offset from the respective VBM position. Figure 2G shows the plots of the resulting positions of E_F, VBM, and CBM for *p*- and *n*-InAs NCs, which yielded the opposite FET characteristics shown in Fig. 1. No substantial change in the position of E_F was observed for either the *p*- or *n*-InAs NCs. A notable difference was observed in the VBM between the *n*- and *p*-InAs NCs. Overall, it was found that the E_F level for the *p*-InAs NC film was closer to its VBM, whereas that for the *n*-InAs NC film was closer to its CBM. This indicates that holes are the majority carriers for the *p*-InAs NCs and electrons for the *n*-InAs NCs, which is consistent with the FET characteristics of the respective NC films shown in Fig. 1.

Additional insights could be acquired from the high-resolution XPS scans of the In and As peaks (Fig. 2H). The binding energies of In $3d_{3/2}$ and $3d_{5/2}$ in the *p*-InAs NCs (451.6 and 444.0 eV, respectively) are smaller than those in *n*-InAs NCs (451.9 and 444.3 eV, respectively). Likewise, the binding energies of As $3d_{3/2}$ and $3d_{5/2}$ were smaller in the *p*-InAs NCs (41.15 and 40.45 eV) compared to those in the *n*-InAs NCs (41.65 and 40.95 eV, respectively). These results indicate that the presence of Zn lowered the binding energies of In and As within the lattice. Lowering the binding energy of the host semiconductor upon *p*-type doping with substitutional acceptors has been widely observed (*45*, *46*). These results support that the Zn present in the *p*-InAs NCs substitutes the In sites in the lattice.

Substitution of larger In (tetrahedral covalent radius = 1.44 Å) with smaller Zn (tetrahedral covalent radius = 1.31 Å) in the InAs NCs yields a contraction in the lattice constant (*47*). This can be verified from a closer look at the diffractogram shown in Fig. 1B. For example, a magnified plot of the prominent (111) peak in the diffractograms of the *p*- and *n*-InAs NCs is shown in fig. S8. The diffraction peak of the *p*- InAs NC (26.0°) is at a larger two-theta value compared to that of the *n*-InAs NCs (25.7°). The associated lattice constants of the InAs NCs can be estimated from the peak positions. The lattice constant for *p*-InAs NCs was 5.92 Å, which is smaller than 6.00 Å of the *n*-InAs NCs. Consistent results are found for the (220) and (311) peaks in the diagram (fig. S8 and table S1). These results indicate the contraction of the lattice structure in the presence of Zn. In addition, the XRD data could be used to quantify the substitution of Zn using an equation describing the size effect of impurities on the lattice constant: $\Delta a/a = \beta_{size} N_i$ (*48*–*50*). Here, a is the lattice constant, Δa is the difference between the lattice constants, β_{size} is the contraction coefficient given as $(r_i - r_h)/(r_h \times N_h)$ (where r_i is the tetrahedral covalent radius of the impurity element (that is, Zn), r_h is the tetrahedral covalent radius of the host element (that is, In), N_h is the concentration of the host atom), and N_i is the concentration of the impurity (*48*–*50*). From this relation, it was found that the Zn/In ratio for the *p*-InAs NCs is 0.17, indicating that 15% of In atoms in the lattice NCs are substituted with Zn. We comment that Zn doping here to InAs NCs is done at a colossal degree, compared to the parts-per-million-level doping in conventional semiconductors.

In addition, extended absorption fine structure (EXAFS) analysis was carried out on both *p*- and *n*-InAs NCs to explore the local bonding environments of In, As, and Zn within each sample. The K-edge Fourier transformed EXAFS spectra for these NCs are displayed in Fig. 2I and fig. S9. Both the In and As K-edge EXAFS spectra for *p*- and *n*-InAs NCs could be successfully fitted using a single In-As scattering path. Details of the fitting are described in Materials and Methods. The structural parameters extracted from the fitting are summarized in table S2. The fitting results indicated a slightly shorter In-As bond length for *p*-InAs NCs compared to *n*-InAs NCs, consistent with the lattice contraction indicated by powder XRD peak shifts. The Zn K-edge EXAFS spectra provided insights into the Zn position for *p*-InAs NCs. Two distinct peaks were observed (Fig. 2I). The peak at a radial distance (R) of 2.424 Å is assigned to the Zn-As scattering path, in line with comparisons to the peak position for bulk Zn_3As_2 powder (fig. S9). This strongly supports the existence of a Zn-As chemical environment within the *p*-InAs NCs, indicating substitutional doping of Zn into an In site (*26*). Meanwhile, the peak at R = 2.096 Å corresponds to Zn coordinating with the amines of the surface ligands or Zn forming oxides. Note that distinguishing between Zn-N and Zn-O scattering paths can be challenging due to their similar EXAFS feature (*51*).

With both *n*-and *p*-InAs NCs available, we demonstrated the fabrication of complementary logic based on these NCs. Figure 3A shows a schematic of the fabrication of complementary logic (for example, a NOT logic gate, also referred to as an inverter). Here, Al_2O_3 was used (instead of SiO_2 used in Fig. 1) as the gate dielectric, and chromium and gold (Cr/Au) were used (instead of Si^{++} used in Fig. 1) as the gate electrodes, both of which were patterned using a conventional lithographic protocol. It should be emphasized that not only is the availability of both *p*- and *n*-type channel materials necessary, but also an appropriate patterning method to place these materials at the designated channel positions is critical for fabricating complementary logic. This was achieved through direct photolithography of NCs using an additive that can crosslink the ligands of neighboring NCs under exposure to UV light, referred to as the 6-light-induced ligand crosslinkers [6-LiXers, that is, 2-(((4-azido-2,3,5,6-tetrafluorobenzoyl)oxy)methyl)-2-((3-((4-azido-2,3,5,6-tetrafluorobenzoyl)oxy)-2,2-bis(((4-azido-2,3,5,6-tetrafluorobenzoyl)oxy)methyl)propoxy)methyl)propane-1,3-diylbis(4-azido-2,3,5,6-tetrafluorobenzoate)]. The chemical structure of 6-LiXer is shown in Fig. 3B. *p*- and *n*-InAs NCs were sufficiently crosslinked even with 1 wt % 6-LiXer (fig. S10). Note that this small content of 6-LiXer marginally affected the electrical characteristics of the InAs NC channels, because the additives were removed eventually after the direct photolithography during the EDT treatment (fig. S11).

Briefly, we first spin-coated *p*-InAs NCs with 1 wt % of 6-LiXers onto substrates prepatterned with a Cr/Au gate electrode and Al_2O_3 gate dielectric. The *p*-channel regimes in the circuit were selectively exposed to a 254-nm UV source. This led to the activation of the azides in LiXer to undergo a C—H insertion reaction with the neighboring NC ligands and form a crosslinked network of NCs. Once the crosslinked network was formed, these regimes in the film remained intact upon dipping the entire film into fresh toluene, while the other non-crosslinked regimes of the film were removed entirely (Fig. 3C). Subsequently, *n*-InAs NCs were photopatterned using the same protocol. The resulting *n*- and *p*-channel regimes were then treated simultaneously with EDT to enhance the electronic coupling between neighboring NCs, as discussed above. Figure 3D shows the C—H stretching absorption peaks of the crosslinked *n*- and *p*-InAs NC films estimated using Fourier transform infrared spectroscopy (FTIR). We can confirm that 90% of OLA ligands exchange with EDT in both *n*- and *p*-InAs NC films. Figure 3E shows

Downloaded from https://www.science.org on December 15, 2023

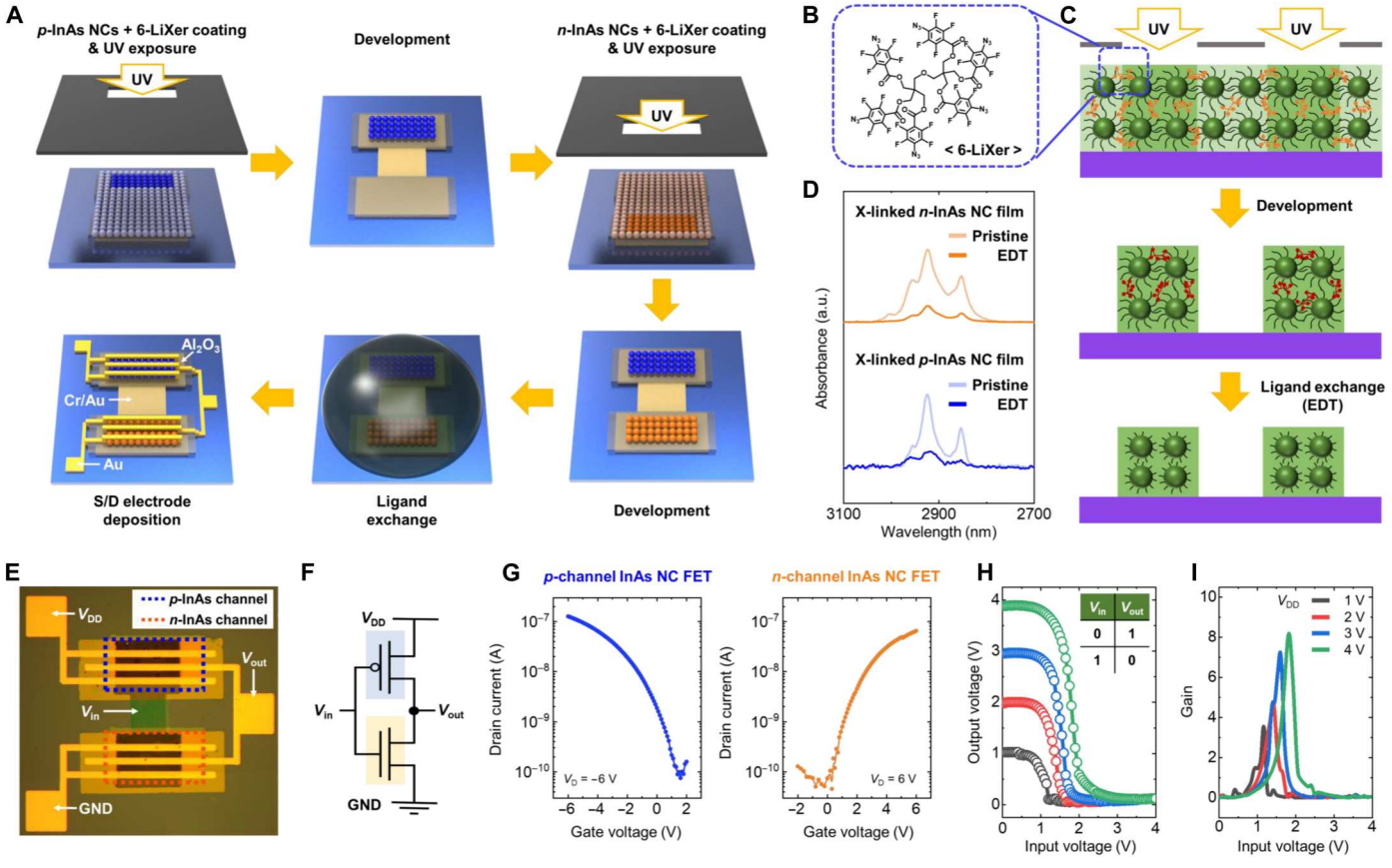

Fig. 3. Complementary NOT logic gate based on photopatterned *p*- and *n*- InAs NCs thin films. (**A**) Schematic description of the process for fabricating complementary logic (e.g., NOT logic). (**B**) Chemical structure of 6-LiXer. (**C**) Schematic description of the patterning process for *p*- and *n*-channels followed by the ligand exchange step. (**D**) FTIR data before and after exchanging ligands of *n*- and *p*-InAs NC films. (**E**) Photograph of the resulting NOT logic. (**F**) Circuitry diagram of the NOT logic. (**G**) Transfer characteristics of patterned *n*- and-*p*-channels. (**H**) Output voltage and (**I**) gain of the NOT gate according to the input signal. S/D, Source and Drain. GND, Ground.

a photograph of the resulting complementary logic fabricated using these steps. Figure 3F depicts the circuitry of the complementary NOT logic. Before the operation of the logic, we examined the transistor characteristics of *n*- and *p*-channels separately. Figure 3G shows the transfer characteristics of *p*- and *n*-channels. Owing to the larger specific capacitance of Al_2O_3 (~100 nF/cm^2) compared to SiO_2 (11.5 nF/cm^2), these devices could operate at lower voltages (6 V), yielding charge carrier mobility values comparable to those shown in Fig. 1. The device parameters are presented in Table 1.

On the basis of the *n*- and *p*-channels exhibiting comparable mobility values, the NOT logic gate was operated at a fixed supply voltage (V_{DD}). The left of Fig. 3H shows the output signals of the NOT logic gate in response to the given input signals under different positive V_{DD}s (1, 2, 3, and 4 V). Here, the input logic state of "0" [defined as a condition with the input voltage (V_{in}) to the circuit being equal to 0 V] was inverted to the output logic state of "1" [defined as the condition where the output voltage (V_{out}) of the circuit is equal to V_{DD}]. Conversely, the input logic state of "1" (defined as a condition with $V_{in} = V_{DD}$) was inverted to the output logic state of "0" (defined as the condition with $V_{out} = 0$ V). Figure 3I shows the gain of the inverter ($G = |dV_{out}/dV_{in}|$). G was greater than 8 when $V_{DD} = 4$ V. The butterfly curves (the mirrored voltage curve) to extract the static noise margin of the NOT logic are shown in fig. S12.

The fabrication of complementary logic can be expanded to logic gates comprising two *n*-channels and two *p*-channels. Figure 4A shows circuit diagrams of the NAND and NOR comprising two *n*-channels and two *p*-channels connected differently. Similar to the fabrication steps shown in Fig. 3A, the fabrication was performed by (i) prepatterning the gate and gate dielectric, (ii) forming two *p*-channels (by photopatterning *p*-InAs NCs with the aid of 6-LiXer), (iii) forming two *n*-channels (by photopatterning *n*-InAs NCs with the aid of 6-LiXer), (iv) exchange of ligands of NCs for the *p*- and *n*-channels using EDT, and (v) depositing top source/drain electrodes (Fig. 4B). Figure 4C shows the photographs of the resulting logic gates. For these logic gates, two input signals ($V_{in,A}$, $V_{in,B}$) were applied with different combinations of logic states, whereas V_{DD} was fixed at 3 V: (V_A, V_B) = (0, 0), (1, 0), (0, 1), and (1, 1) (Fig. 4D). Again, the input logic state of "0" here is defined as $V_{in} = 0$ V, while that of "1" is defined as $V_{in} = V_{DD}$. Figure 4E shows the output signals of the NAND gate for the respective combinations of input signals. The output logic state was "0" only when (V_A, V_B) = (1, 1) was applied (that is, when both $V_{in,A}$ and $V_{in,B}$ were in the logic state of "1"), whereas the other input combinations such as (V_A, V_B) = (0, 0), (1, 0), and (0, 1) yielded the

Downloaded from https://www.science.org on December 15, 2023

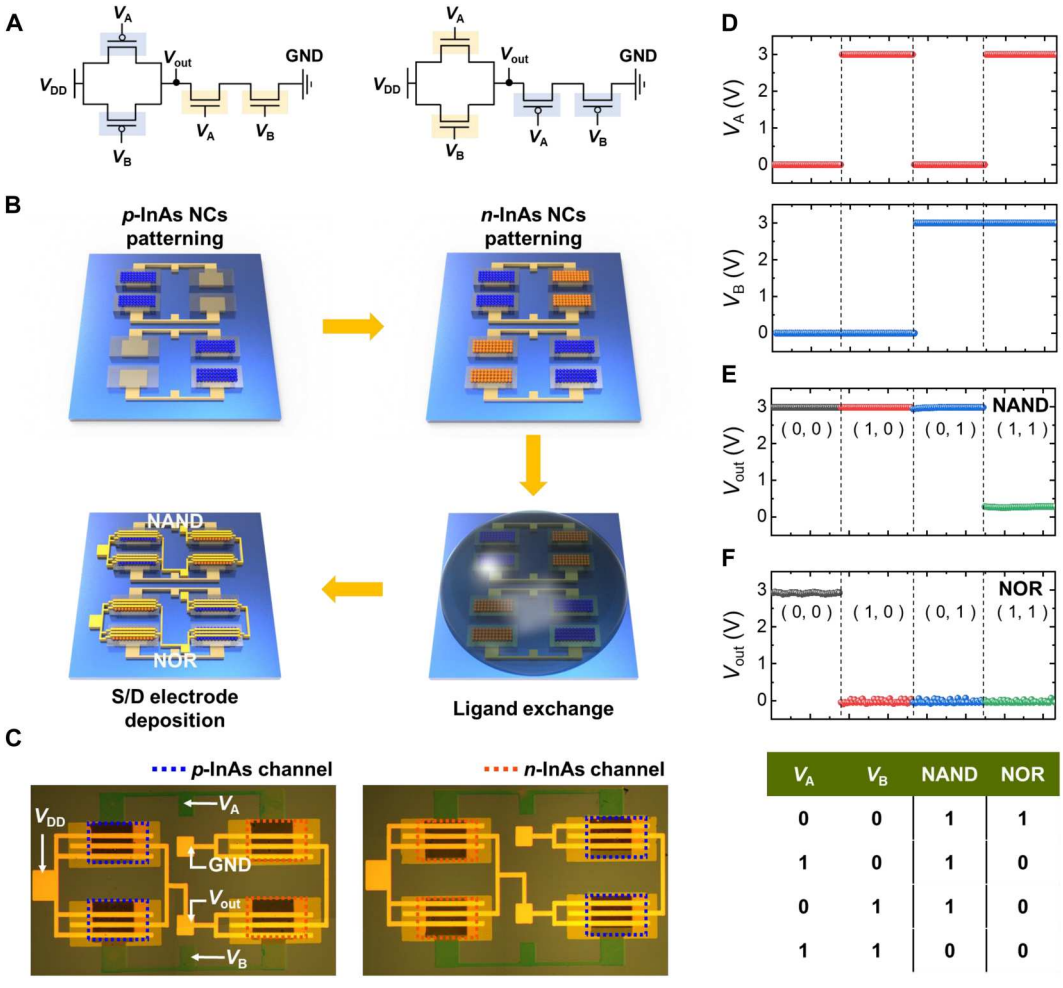

V_A	V_B	NAND	NOR
0	0	1	1
1	0	1	0
0	1	1	0
1	1	0	0

Fig. 4. NAND and NOR logic gates based on photopatterned *p*- and *n*- InAs NCs thin films. (**A**) Circuit diagrams of NAND and NOR logic gates, both of which comprise two *n*- and two *p*-channels. (**B**) Schematic description of the process for fabricating complementary NAND and NOR logic gates. (**C**) Photographs of NAND and NOR logic gates. (**D**) Input signals applied to the logic gates. (**E**) Output signals of the NAND logic. (**F**) Output signals of the NOR logic gate.

output logic state of "1". Evidently, the circuit operates as NAND logic. Figure 4F, in contrast, shows the output signals of the NOR gate under respective combinations of input signals. In this case, the output logic state was "0" when (V_A, V_B) = (1, 0), (0, 1), or (1, 1) (that is, when either $V_{in,\ A}$ or $V_{in,\ B}$ was in the logic state of "1"), whereas (V_A, V_B) = (0, 0) (that is, when none of $V_{in,\ A}$ and $V_{in,\ B}$ was in the logic state of "1") yielded the output logic state of "1" clearly demonstrating the NOR operation of the logic.

DISCUSSION

We show that InAs NCs with either *p*- or *n*-type semiconductor characteristics can be prepared directly from the syntheses using aminoarsine precursors with different reducing agents to activate As precursors. The use of DIBAL-H yielded *n*-type InAs NCs, whereas the use of Et_2Zn resulted in the inclusion of Zn within the InAs lattice to produce *p*-type InAs NCs. This is the first NC system capable of controlling semiconductor polarity with heteroatoms at the synthesis level leading to apparent hole and electron transport behavior at the device level. Having both *p*- and *n*-type InAs NCs in the material library, we successfully fabricated complementary logic, including NOT, NOR, and NAND. We consider that the RoHS-compliant, polarity-controlled InAs NC system allows the wider use of NCs in electronic/optoelectronic applications.

MATERIALS AND METHODS

Materials

For NC synthesis, $InCl_3$ (98%, Sigma-Aldrich), DMA-As (99%, Strem), Et_2Zn solution (1 M in hexane, Sigma-Aldrich), DIBAL-H solution (1 M in toluene, Sigma-Aldrich), trioctylphosphine (TOP, 97%, Uniam), and anhydrous solvents (hexane, toluene, and 1-butanol, Sigma-Aldrich) were used without further purification. OLA (technical grade, 70%, Sigma-Aldrich) was purified by distillation and stored in a glove box. For the solid-state ligand-exchange step, EDT (98%, Sigma-Aldrich), ammonium chloride (NH_4Cl, 99.5%, Sigma-Aldrich), ammonium bromide (NH_4Br, 99%, Sigma-Aldrich), ammonium iodide (NH_4I, 99%, Sigma-Aldrich), sodium sulfide (Na_2S, Sigma-Aldrich), acetonitrile (electronic grade, 99.999%, Sigma-Aldrich), and methanol (anhydrous, 99.8%) were used without further purification. The 6-LiXers were

Downloaded from https://www.science.org on December 15, 2023

synthesized according to a previously reported method (*52*, *53*). For FETs, Si wafers (n^{++}, <0.005 ohm) with a thermally grown SiO_2 layer (300 nm) (Namkang Hi-Tech) were used as the substrate. Aluminum nitrate nonahydrate (98%, Sigma-Aldrich) and 2-methoxyethanol (anhydrous, 99.8%, Sigma-Aldrich) were used as the precursors of Al_2O_3 dielectrics for complementary logic. A buffer oxide etchant (BOE; 6:1, Sigma-Aldrich) was used to etch the Al_2O_3 dielectrics.

Synthesis of *n*-InAs NCs

n-InAs NCs were synthesized using a modified method reported by Srivastava *et al.* (*29*). For a typical synthesis, In precursor solution was prepared by degassing 3 mmol of $InCl_3$ in OLA (15 ml). The As precursor solution was prepared separately by adding 1.5 mmol of DMA-As to OLA (1 ml). After degassing, the In precursor solution was heated up to 270°C under a nitrogen atmosphere, and the As precursor solution was injected into the former, followed by injection of DIBAL-H solution (1 ml). The reaction solution was kept at 270°C for 1 hour and then cooled to room temperature. The as-synthesized NCs were purified using hexane and 1-butanol in a nitrogen-filled glove box and were redispersed in toluene for further use.

Synthesis of *p*-InAs NCs

For a typical synthesis, In precursor solution was prepared by degassing 0.5 mmol of $InCl_3$ in OLA (8 ml). Separately, the As precursor solution was prepared by mixing 0.3 mmol of DMA-As in OLA (0.8 ml), TOP (0.5 ml), and the Et_2Zn solution (0.6 ml). The mixture was then heated to 240°C for 10 min and cooled down to room temperature. Next, the As precursor solution was introduced to the In precursor solution at room temperature and was heated up to 160°C for 10 min. Subsequently, the reaction mixture was further heated up to 320°C with the additional introduction of In and As precursor solutions (In/As ratio = 0.8, injection rate = 0.1 ml/min). The resulting *p*-InAs NCs were purified using hexane and 1-butanol in a nitrogen-filled glove box and were redispersed in toluene.

Device fabrication

Cr/Au (5/50 nm) electrodes were thermally deposited through a shadow mask onto a heavily *n*-doped Si substrate with a 300-nm-thick thermally grown SiO_2 layer. InAs NCs dispersed in toluene (10 mg/ml) were spin-coated at 2000 rpm for 30 s. For ligand exchange, the NC films were treated with 50 mM EDT in acetonitrile for 30 s and then rinsed twice with fresh acetonitrile, followed by annealing at 220°C for 30 min.

For transistors in the logic gates, aluminum nitrate nonahydrate (98%, Sigma-Aldrich) dissolved in 2-methoxyethanol (anhydrous, 99.8%, Sigma-Aldrich) at a concentration of 0.5 M was used as the precursor for Al_2O_3 dielectrics. The mixture solution was stirred with a magnetic bar for 24 hours at 65°C and then spin-coated (4000 rpm, 30 s) onto a UV-treated Si/SiO_2 wafer prepatterned with Cr/Au (3/17 nm) gate electrode, which was thermally deposited through a shadow mask. The precursor film was annealed at 500°C for 2 hours in a furnace. The resulting Al_2O_3 gate dielectric layer (thickness = 50 nm, specific capacitance = 100 nF/cm^2) was patterned via conventional photolithography and wet etching using BOE (8 s). A mixture of *p*-InAs NCs containing 6-LiXer (1 wt % relative to the weight of the NCs) in toluene (10 mg/ml) was spin-coated (2000 rpm for 30 s) onto the wafer. Subsequently, the channel regimes of the transistors were selectively irradiated with UV (254 nm, 0.4 mW/cm^2, corresponding exposure 2 mJ/cm^2) through a photomask for 10 s. UV irradiation resulted in crosslinking of the ligands on the NC surface. The *p*-channel patterns were formed by removing the uncrosslinked regime of the film using toluene. The *n*-channel patterns were subsequently formed using *n*-InAs NCs following the same protocol to form *p*-channel patterns. Once *p*- and *n*-InAs NCs were patterned, the ligands of these NCs were replaced with EDT by treating the patterns with 50 mM EDT in acetonitrile for 30 s (followed by rinsing with fresh acetonitrile and annealing at 220°C for 30 min). Last, Au (50 nm) source/drain top electrodes were thermally deposited on the channels.

Characterization

UV-VIS-NIR absorbance spectra of *p*- and *n*-InAs NCs were obtained using an UV-3600 (Shimadzu) at the Chiral Material Core Facility Center of Sungkyunkwan University. Transmission electron microscopy images of *p*- and *n*-InAs NCs were obtained using a JEM-ARM200CF instrument (JEOL). XRD measurements were performed using a Miniflex 600 (Rigaku) instrument. FTIR spectra were collected using an iS10 FTIR spectrometer (Thermo Fisher Scientific). XPS measurements for films of *p*- and *n*-InAs NCs were carried out using a NEXSA (Thermo Fisher Scientific). For XPS measurements, films were prepared on a Si substrate coated with a Cr/Au (5/70 nm) layer. Binding energies were calibrated using the C1s core level (284.8 eV). APS measurements for films of *p*- and *n*-InAs NCs were performed using an APS04 system (KP Technology). Kelvin probe measurements were performed using a Park NX10 (Park Systems). The work function of the tip was calibrated using highly oriented pyrolytic graphite (work function = 4.48 eV). Electrical measurements of the resulting devices were performed inside a vacuum probe station (MSTECH M5VC) connected to a Keithley 4200-SCS parameter analyzer.

Synchrotron-based x-ray absorption spectroscopy (XAS) measurements were performed at Pohang Accelerator Laboratory (PAL-10C beamline). Before the measurement, the specimens were prepared in a nitrogen-filled glove box, deposited on Scotch tape, overlapped two times, and mounted on a sample holder. The XAS measurements were carried out at the In, As, and Zn K-edge, using both transmission and fluorescence modes. Pre- and post-edge background subtraction and normalization were performed using the ATHENA software. The obtained XAS spectra were plotted and analyzed using the ATHENA and ARTEMIS software, respectively. For the In and As K-edge EXAFS analysis, we used In-As scattering path covering *k*-space ranging from 3.0 to 12.0 Å^{-1}, *R*-space spanning from 1.5 to 3.0 Å, and R_{bkg} of 1.0 Å. In the case of Zn K-edge EXAFS data of *p*-InAs NCs, fitting involved Zn-O and Zn-As scattering paths in *k*-space ranging from 2.0 to 11.0 Å^{-1}, *R*-space spanning from 1.45 to 3.00 Å, and R_{bkg} of 1.4 Å. The best fits were achieved when both paths were used. Although we used the first coordination shell of Zn-O scattering path for fitting, we acknowledge the challenge of distinguishing between Zn-O (resulting from surface oxidation) and Zn-N (resulting from amine ligand-surface coordination) scattering paths due to their similar EXAFS feature (*51*). Therefore, quantifying the contribution of oxidized Zn remains elusive. All scattering paths were generated using FEFF6 calculation. S_0^2 values for In, As, and Zn were obtained by reference values as 0.82, 0.66, and 0.839,

Downloaded from https://www.science.org on December 15, 2023

respectively (*26*). Coordination number (CN), bond length (*R*), and mean square relative displacement (σ^2) were treated as variables.

Simulation

We performed first-principles DFT calculations to investigate the stability of the Zn defects in the InAs NCs. The atomic structure of NCs was fully relaxed by using the exchange-correlation functional PBE suggested by Perdew, Burke, and Ernzerhof. Subsequently, self-consistent field calculation was performed by using the hybrid functional HSE06 suggested by Heyd, Scuseria, and Ernzerhof (*54*). For the description of electron-ion interaction, we used the projector-augmented wave method as implemented in the Vienna Ab initio simulation package (*55*, *56*). We generated two model NCs, that is, $In_{55}As_{68}$ and $In_{79}As_{80}$, and surface dangling bonds were passivated by pseudo-hydrogen atoms (fig. S13). The maximum distances between the atoms in the smaller and the larger NCs were 18.1 and 20.5 Å, respectively. The bandgaps of the smaller and the larger NCs were 2.36 and 2.19 eV, respectively, larger than the electronic bandgap of bulk InAs of 0.38 eV due to the quantum confinement effect. For charged defect calculations, the correction scheme FNV suggested by Freysoldt, Neugebauer, and Van de Walle was used, and the convergence of the formation energy was examined using larger supercells. The cell size was sufficiently large to obtain converged formation energy (fig. S14). The acceptor level of the substitutional Zn defect is 0.83 and 1.22 eV in the larger and the smaller NCs, respectively. As the quantum confinement effect weakened, both the bandgap and the acceptor level decreased and converged to the bulk values of 0.38 and 0.10 eV, respectively.

Supplementary Materials

This PDF file includes:

Figs S1 to S14
Tables S1 and S2
Supplementary Text

REFERENCES AND NOTES

1. C. R. Kagan, E. Lifshitz, E. H. Sargent, D. V. Talapin, Building devices from colloidal quantum dots. *Science* **353**, aac5523 (2016).
2. Directive 2011/65/EU of the european parliament and of the the council, European Union. *O.J. L* **174**, 88–110 (2011).
3. Y. Kim, J. H. Chang, H. Choi, Y. H. Kim, W. K. Bae, S. Jeong, III-V colloidal nanocrystals: Control of covalent surfaces. *Chem. Sci.* **11**, 913–922 (2020).
4. L. A. Cipriano, G. Di Liberto, S. Tosoni, G. Pacchioni, Quantum confinement in group III-V semiconductor 2D nanostructures. *Nanoscale* **12**, 17494–17501 (2020).
5. X. L. Dai, Y. Z. Deng, X. G. Peng, Y. Z. Jin, Quantum-dot light-emitting diodes for large-area displays: Towards the dawn of commercialization. *Adv. Mater.* **29**, 1607022 (2017).
6. E. Jang, IEEE: Paper presented at the 64th Annual Meeting of the IEDM, San Francisco, CA, December (2018).
7. M. Soreni-Harari, D. Mocatta, M. Zimin, Y. Gannot, U. Banin, N. Tessler, Interface modifications of InAs quantum-dots solids and their effects on FET performance. *Adv. Funct. Mater.* **20**, 1005–1010 (2010).
8. W. Y. Liu, J. S. Lee, D. V. Talapin, III-V nanocrystals capped with molecular metal chalcogenide ligands: High electron mobility and ambipolar photoresponse. *J. Am. Chem. Soc.* **135**, 1349–1357 (2013).
9. J. H. Song, H. Choi, H. T. Pham, S. Jeong, Energy level tuned indium arsenide colloidal quantum dot films for efficient photovoltaics. *Nat. Commun.* **9**, 4267 (2018).
10. H. B. Jalali, L. De Trizio, L. Manna, F. Di Stasio, Indium arsenide quantum dots: An alternative to lead-based infrared emitting nanomaterials. *Chem. Soc. Rev.* **51**, 9861–9881 (2022).
11. T. Kim, D. Shin, M. Kim, H. Kim, E. Cho, M. Choi, J. Kim, E. Jang, S. Jeong, Development of group III-V colloidal quantum dots for optoelectronic applications. *ACS Energy Lett.* **8**, 447–456 (2023).
12. H. Zhang, J. Jang, W. Y. Liu, D. V. Talapin, Colloidal nanocrystals with inorganic halide, pseudohalide, and halometallate ligands. *ACS Nano* **8**, 7359–7369 (2014).
13. D. C. Tripathi, L. Asor, G. Zaharoni, U. Banin, N. Tessler, Surface versus impurity-doping contributions in InAs nanocrystal field effect transistor performance. *J. Phys. Chem. C* **123**, 18717–18725 (2019).
14. J. Leemans, V. Pejovic, E. Georgitzikis, M. Minjauw, A. Siddik, Y. H. Deng, Y. H. Kuang, G. Roelkens, C. Detavernier, I. Lieberman, P. E. Malinowski, D. Cheyns, Z. Hens, Colloidal III-V quantum dot photodiodes for short-wave infrared photodetection. *Adv. Sci.* **9**, 2200844 (2022).
15. T. S. Zhao, Q. H. Zhao, J. Y. Lee, S. S. Yang, H. Wang, M. Y. Chuang, Y. L. He, S. M. Thompson, G. N. Liu, N. Oh, C. B. Murray, C. R. Kagan, Engineering the surface chemistry of colloidal InP quantum dots for charge transport. *Chem. Mater.* **34**, 8306–8315 (2022).
16. M. Noguchi, K. Hirakawa, T. Ikoma, Intrinsic electron accumulation layers on reconstructed clean InAs(100) surfaces. *Phys. Rev. Lett.* **66**, 2243–2246 (1991).
17. A. Hoglund, C. W. M. Castleton, M. Gothelid, B. Johansson, S. Mirbt, Point defects on the (110) surfaces of InP, InAs, and InSb: A comparison with bulk. *Phys. Rev. B* **74**, 075332 (2006).
18. D. K. Kim, Y. M. Lai, B. T. Diroll, C. B. Murray, C. R. Kagan, Flexible and low-voltage integrated circuits constructed from high-performance nanocrystal transistors. *Nat. Commun.* **3**, 1216 (2012).
19. F. S. Stinner, Y. M. Lai, D. B. Straus, B. T. Diroll, D. K. Kim, C. B. Murray, C. R. Kagan, Flexible, high-speed CdSe nanocrystal integrated circuits. *Nano Lett.* **15**, 7155–7160 (2015).
20. H. J. Yun, J. Lim, J. Roh, D. C. J. Neo, M. Law, V. I. Klimov, Solution-processable integrated CMOS circuits based on colloidal $CuInSe_2$ quantum dots. *Nat. Commun.* **11**, 5280 (2020).
21. B. N. Pal, I. Robel, A. Mohite, R. Laocharoensuk, D. J. Werder, V. I. Klimov, High-sensitivity p-n junction photodiodes based on PbS nanocrystal quantum dots. *Adv. Funct. Mater.* **22**, 1741–1748 (2012).
22. J. Tang, H. Liu, D. Zhitomirsky, S. Hoogland, X. H. Wang, M. Furukawa, L. Levina, E. H. Sargent, Quantum junction solar cells. *Nano Lett.* **12**, 4889–4894 (2012).
23. T. Kim, S. Lim, S. Yun, S. Jeong, T. Park, J. Choi, Design strategy of quantum dot thin-film solar cells. *Small* **16**, e2002460 (2020).
24. S. M. Geyer, P. M. Allen, L. Y. Chang, C. R. Wong, T. P. Osedach, N. Zhao, V. Bulovic, M. G. Bawendi, Control of the carrier type in InAs nanocrystal films by predeposition incorporation of Cd. *ACS Nano* **4**, 7373–7378 (2010).
25. L. Asor, J. Liu, Y. Ossia, D. C. Tripathi, N. Tessler, A. I. Frenkel, U. Banin, InAs nanocrystals with robust p-type doping. *Adv. Funct. Mater.* **31**, 2007456 (2021).
26. L. Asor, J. Liu, S. Xiang, N. Tessler, A. I. Frenkel, U. Banin, Zn-doped p-type InAs nanocrystal quantum dots. *Adv. Mater.* **35**, e2208332 (2023).
27. V. Grigel, D. Dupont, K. De Nolf, Z. Hens, M. D. Tessier, InAs colloidal quantum dots synthesis via aminopnictogen precursor chemistry. *J. Am. Chem. Soc.* **138**, 13485–13488 (2016).
28. V. Srivastava, E. M. Janke, B. T. Diroll, R. D. Schaller, D. V. Talapin, Facile, economic and size-tunable synthesis of metal arsenide nanocrystals. *Chem. Mater.* **28**, 6797–6802 (2016).
29. V. Srivastava, E. Dunietz, V. Kamysbayev, J. S. Anderson, D. V. Talapin, Monodisperse InAs quantum dots from aminoarsine precursors: Understanding the role of reducing agent. *Chem. Mater.* **30**, 3623–3627 (2018).
30. J. B. Zhang, D. L. Zhang, Synthesis and growth kinetics of high quality InAs nanocrystals using in situ generated AsH_3 as the arsenic source. *CrstEngComm* **12**, 591–594 (2010).
31. J. B. Zhang, D. L. Zhang, Photoluminescence and growth kinetics of high-quality indium arsenide and InAs-based core/shell colloidal nanocrystals synthesized using arsine (AsH_3) generated via zinc arsenide as the arsenic source. *Chem. Mater.* **22**, 1579–1584 (2010).
32. D. Battaglia, X. G. Peng, Formation of high quality InP and InAs nanocrystals in a non-coordinating solvent. *Nano Lett.* **2**, 1027–1030 (2002).
33. R. G. Xie, X. G. Peng, Synthetic scheme for high-quality InAs nanocrystals based on self-focusing and one-pot synthesis of InAs-based core-shell nanocrystals. *Angew. Chem.Int. Ed.* **47**, 7677–7680 (2008).
34. S. Tamang, S. Lee, H. Choi, S. Jeong, Tuning size and size distribution of colloidal InAs nanocrystals via continuous supply of prenucleation clusters on nanocrystal seeds. *Chem. Mater.* **28**, 8119–8122 (2016).
35. T. Kim, S. Park, S. Jeong, Diffusion dynamics controlled colloidal synthesis of highly monodisperse InAs nanocrystals. *Nat. Commun.* **12**, 3013 (2021).
36. D. X. Zhu, F. Bellato, H. B. Jalali, F. Di Stasio, M. Prato, Y. P. Ivanov, G. Divitini, I. Infante, L. De Trizio, L. Manna, $ZnCl_2$ Mediated synthesis of InAs nanocrystals with aminoarsine. *J. Am. Chem. Soc.* **144**, 10515–10523 (2022).
37. D. V. Talapin, C. B. Murray, PbSe nanocrystal solids for n- and p-channel thin film field-effect transistors. *Science* **310**, 86–89 (2005).

Downloaded from https://www.science.org on December 15, 2023

38. K. S. Leschkies, M. S. Kang, E. S. Aydil, D. J. Norris, Influence of atmospheric gases on the electrical properties of PbSe quantum-dot films. *J. Phys. Chem. C* **114**, 9988–9996 (2010).
39. D. Bederak, D. M. Balazs, N. V. Sukharevska, A. G. Shulga, M. Abdu-Aguye, D. N. Dirin, M. V. Kovalenko, M. A. Loi, Comparing halide ligands in PbS colloidal quantum dots for field-effect transistors and solar cells. *ACS Appl. Nano Mater.* **1**, 6882–6889 (2018).
40. S. Kim, S. N. Hood, J. S. Park, L. D. Whalley, A. Walsh, Quick-start guide for first-principles modelling of point defects in crystalline materials. *J. Phys Energy* **2**, 036001 (2020).
41. A. C. Ford, S. Chuang, J. C. Ho, Y. L. Chueh, Z. Y. Fan, A. Javey, Patterned p-doping of InAs nanowires by gas-phase surface diffusion of Zn. *Nano Lett.* **10**, 509–513 (2010).
42. G. S. Shao, Work function and electron affinity of semiconductors: Doping effect and complication due to fermi level pinning. *Energy Environ. Mater.* **4**, 273–276 (2021).
43. J. Jasieniak, M. Califano, S. E. Watkins, Size-dependent valence and conduction band-edge energies of semiconductor nanocrystals. *ACS Nano* **5**, 5888–5902 (2011).
44. K. K. Hisao Ishii, Takashi Nakayama, Nobuo Ueno, *Electronic Processes in Organic Electronics* (Springer, 2015).
45. J. Hedman, Y. Baer, A. Berndtsson, M. Klasson, G. Leonhardt, R. Nilsson, C. Nordling, Influence of doping on the electron spectrum of silicon. *J. Electron. Spectrosc. Relat. Phenom.* **1**, 101–104 (1972).
46. T. Higuchi, T. Tsukamoto, N. Sata, M. Ishigame, Y. Tezuka, S. Shin, Electronic structure of *p*-type $SrTiO_3$ by photoemission spectroscopy. *Phys. Rev. B* **57**, 6978 (1998).
47. P. Pyykko, Refitted tetrahedral covalent radii for solids. *Phys. Rev. B* **85**, (2012).
48. C. G. Van de Walle, Effects of impurities on the lattice parameters of GaN. *Phys. Rev. B* **68**, 165209 (2003).
49. D. Mocatta, G. Cohen, J. Schattner, O. Millo, E. Rabani, U. Banin, Heavily doped semiconductor nanocrystal quantum dots. *Science* **332**, 77–81 (2011).
50. E. Kluth, M. Wieneke, J. Blasing, H. Witte, K. Lange, A. Dadgar, R. Goldhahn, M. Feneberg, The impurity size-effect and phonon deformation potentials in wurtzite GaN. *Semicond. Sci. Technol.* **35**, 095033 (2020).
51. C. Xie, L. Lin, L. Huang, Z. Wang, Z. Jiang, Z. Zhang, B. Han, Zn-Nx sites on N-doped carbon for aerobic oxidative cleavage and esterification of C(CO)-C bonds. *Nat. Commun.* **12**, 4823 (2021).
52. J. Yang, M. Lee, S. Y. Park, M. Park, J. Kim, N. Sitapure, D. Hahm, S. Rhee, D. Lee, H. Jo, Y. H. Jo, J. Lim, J. Kim, T. J. Shin, D. C. Lee, K. Kwak, J. S. Kwon, B. Kim, W. K. Bae, M. S. Kang, Non-destructive photopatterning of heavy-metal-free quantum dots. *Adv. Mater.* **34**, e2205504 (2022).
53. D. Han, M. Lee, W. Jang, S. Lee, J. Yang, H. Jo, H. Lee, K. Kwak, B. Kim, M. S. Kang, Two-Color Strip-Patterned White OLEDs: Tunable Color-Temperature via Pattern Dimension Control. *Adv. Opt. Mater.* **10**, 2200456 (2022).
54. J. P. Perdew, K. Burke, M. Ernzerhof, Generalized Gradient Approximation Made Simple. *Phys. Rev. Lett.* **77**, 3865–3868 (1996).
55. P. E. Blöchl, Projector augmented-wave method. *Phys. Rev. B* **50**, 17953–17979 (1994).
56. G. Kresse, J. Furthmüller, Efficient iterative schemes for *ab initio* total-energy calculations using a plane-wave basis set. *Phys. Rev. B* **54**, 11169–11186 (1996).

Acknowledgments

Funding: This work was supported by the National Research Foundation of Korea (NRF) grant funded by the Ministry of Science, ICT, and Future Planning (NRF-2019M3D1A1078299, 2021R1A2C2008332, and 2022R1A2C2091486). B.K. and J.H.C. were also supported by the Samsung Research Funding and Incubation Center of Samsung Electronics (SRFC-MA1901-51).

Author contributions: J.I.Y. H.K., S.J., and M.S.K. conceived the original idea and designed experiments. J.-S.P. carried out the computational calculation. M.S.K., S.J., and J.-S.P. supervised the work. J.I.Y., H.C., M.C., S.L., and H.J. characterized the semiconductor properties of InAs NCs. H.K., M.K., S.P., and T.K. synthesized the InAs NCs. J.I.Y., Y.A.K., B.K., J.H.C. and M.S.K. fabricated and characterized complementary logic gates. All the authors discussed the results and contributed to the preparation of the paper. **Competing interests:** S.J., M.S.K., H.K., J.I.Y., and H. J. are inventors on a patent application KR-10-2021-0178597. The authors declare that they have no other competing interests. **Data and materials availability:** All data needed to evaluate the conclusions in the paper are present in the paper and/or the Supplementary Materials.

Submitted 18 July 2023
Accepted 10 October 2023
Published 10 November 2023
10.1126/sciadv.adj8276

Downloaded from https://www.science.org on December 15, 2023

Science Advances

P- and *N*-type InAs nanocrystals with innately controlled semiconductor polarity

Jong Il Yoon, Hyoin Kim, Meeree Kim, Hwichan Cho, Yonghyun Albert Kwon, Mahnmin Choi, Seongmin Park, Taewan Kim, Seunghan Lee, Hyunwoo Jo, BongSoo Kim, Jeong Ho Cho, Ji-Sang Park, Sohee Jeong, and Moon Sung Kang

Sci. Adv. **9** (45), eadj8276. DOI: 10.1126/sciadv.adj8276

View the article online
https://www.science.org/doi/10.1126/sciadv.adj8276
Permissions
https://www.science.org/help/reprints-and-permissions

Downloaded from https://www.science.org on December 15, 2023

Use of this article is subject to the Terms of service

Science Advances (ISSN 2375-2548) is published by the American Association for the Advancement of Science. 1200 New York Avenue NW, Washington, DC 20005. The title *Science Advances* is a registered trademark of AAAS.

Copyright © 2023 The Authors, some rights reserved; exclusive licensee American Association for the Advancement of Science. No claim to original U.S. Government Works. Distributed under a Creative Commons Attribution NonCommercial License 4.0 (CC BY-NC).